Elucidating Effects of Orbital Delocalization on Electrochemiluminescent Efficiency for Carbon Nitrides

Yanfeng Fang, Yuhua Hou, Hong Yang, Wang Li, Jin Ma, Dan Han, Xuwen Cao, Songqin Liu, Yanfei Shen, Yuanjian Zhang*

Jiangsu Engineering Laboratory of Smart Carbon-Rich Materials and Device, Jiangsu Province Hi-Tech Key Laboratory for Bio-Medical Research, State Key Laboratory of Bioelectronics, School of Chemistry and Chemical Engineering, Medical School, Southeast University, Nanjing 211189, China.

E-mail: Yuanjian.Zhang@seu.edu.cn

Abstract

Electrochemiluminescence (ECL), an emission of light excited by electrochemical reactions, has drawn attention as tools across diverse fields, ranging from clinical disease diagnosis to photo-/electro-catalysts development. Nonetheless, the ECL efficiency of most luminophores in aqueous solutions is low, which significantly hamper their broad applications; thus, understanding the intrinsic factors for ECL efficiency is highly envisioned. Herein, taking emerging carbon nitride (CN) with unique electronic structures and rigid 2D backbone as a model luminophore, we report that the orbital delocalization was a promising unifying factor for its ECL efficiency. Behind the complicated transformation of molecular structures regarding cyano-terminal groups and triazine/heptazine basal frameworks, the orbital delocalization of the as-prepared CN was found to be generally improved at an elevated condensation temperature. Such intrinsic evolution in electronic structure favored the electron injection in excitation and photon emission afterward in ECL of CN. As a result, the cathodic ECL efficiency of CN was remarkably improved to a new milestone of 170-fold greater than benchmark $Ru(bpy)_3Cl_2$.

Introduction

Highly efficient interconversion of different types of energy is essential not only in living but also for science and technology development. One prominent example is that chlorophyll, enzymes, and Escherichia coli maintain normal physiological function at an extreme efficiency approaching the physical limit. In contrast, there exists a giant gap for artificial devices to pursue. For instance, electrochemiluminescence (ECL), a light emission process in which excited species are generated at electrode surfaces by electrochemical reactions, has been widely applied ranging from clinical disease diagnosis to bioimaging.[1-7] Nonetheless, ECL efficiency (number of generated photons per occupied electrons) of most emitters in aqueous solutions, including the commercialized benchmark tris(2,2′-bipyridyl)ruthenium(II) chloride ($Ru(bpy)_3Cl_2$), is essentially low (typically less than 2%),[8] which significantly hamper their broad applications.

Numerous efforts have been devoted to addressing this problem, e.g., exploring new ECL emitters via screening luminophores with superior photophysical properties.[7, 9-14] Alternatively, the ECL efficiency of existing emitters was enhanced by strengthening intermolecular charger transfer,[15-16] radical stabilization,[17-20], and aggregation effects.[13-14, 21-23] Despite these unprecedented successes, the study of ECL emitters with high ECL efficiency and the associated mechanism is still in infancy. For instance, the reliable correlations between photoluminescent (PL) quantum yield (QY) and ECL efficiency remain controversial,[13, 18, 24] as the excitation kinetics of PL and ECL are different, e.g., the time scale of the former is faster than the latter by up to 6 orders of magnitude. Moreover, in previous studies, the ECL efficiency is often confused with ECL intensity,[25] making the intrinsic comparison among different ECL emitters difficult. Therefore, from both a fundamental and application point of view, it is urgent to understand the intrinsic factors that influence ECL efficiency and consequently make an improvement.

Due to the unique rigid 2D backbone and the associated electronic structures, polymeric carbon nitride (CN) has emerged as a promising new generation of metal-free luminophore.[26-29] It had demonstrated a record cathodic ECL efficiency of ca. seven times of benchmark $Ru(bpy)_3Cl_2$ in an aqueous solution.[30] Herein, taking CN with modulable molecular structures as a model system, we report the physicochemical insights of orbital delocalization on enhancing ECL efficiency by a general kinetic evaluation of electrons and photons participated-processes in ECL. In contrast to PL, it was disclosed that the quantitative orbital delocalization index (ODI), associated with the complicated development of cyano-terminal groups and basal triazine/heptazine frameworks during the thermal condensation of CN, could be regarded as a unified intrinsic factor for Φ_{ECL} of CN. Following this finding, the cathodic ECL efficiency of CN photoelectrode further improved remarkably up to ca. 170 times of benchmark $Ru(bpy)_3Cl_2$.

Results and Discussion

Following our previous work,[30] fluorine-doped tin oxide (FTO) was used as the substrate to absorb microwave energy, on which cyanamide could be rapidly heated and polymerized on FTO (**Figure 1a**). A thermal infrared camera was used to monitor the temperature distribution in real-time during the microwave-assisted synthesis **(Figure 1b and S1)**. As shown in **Movie S1,** the temperature of the reaction system could quickly increase at ca. 60 ^{o}C/s by microwave irradiation. As a result, robust and uniform CN films under different temperatures were successfully grown on FTO in seconds, denoting CN_{MWT} (T= 400 to 720 ^{o}C, see morphology, crystal structures, electronic structures, and chemical bonding of CN_{MWT} in **Figure S2-6**). Notably, CN started to decompose at a temperature higher than 600 ^{o}C (see the thermal image and TGA curves in **Figure S1e and S7**).

The detailed chemical structure of different CN_{MWT} was investigated by Fourier transformed infrared spectroscopy (FT-IR). As shown in **Figure 1c**, the FT-IR spectra of all CN_{MWT} showed the peak at around 800 and 1100-1700 cm^{-1}, typically attributing

to triazine or heptazine ring out of plane bending and the C-N heterocycles stretching vibrations, respectively.[31-32] Notably, characteristic vibrations for ν(−NH_2) at 3457/3325 cm^{-1} and C≡N at 2205 cm^{-1} were observed for CN_{MW400},[33-34] suggesting an incomplete polymerization; at the higher temperature, these terminal groups gradually disappeared.

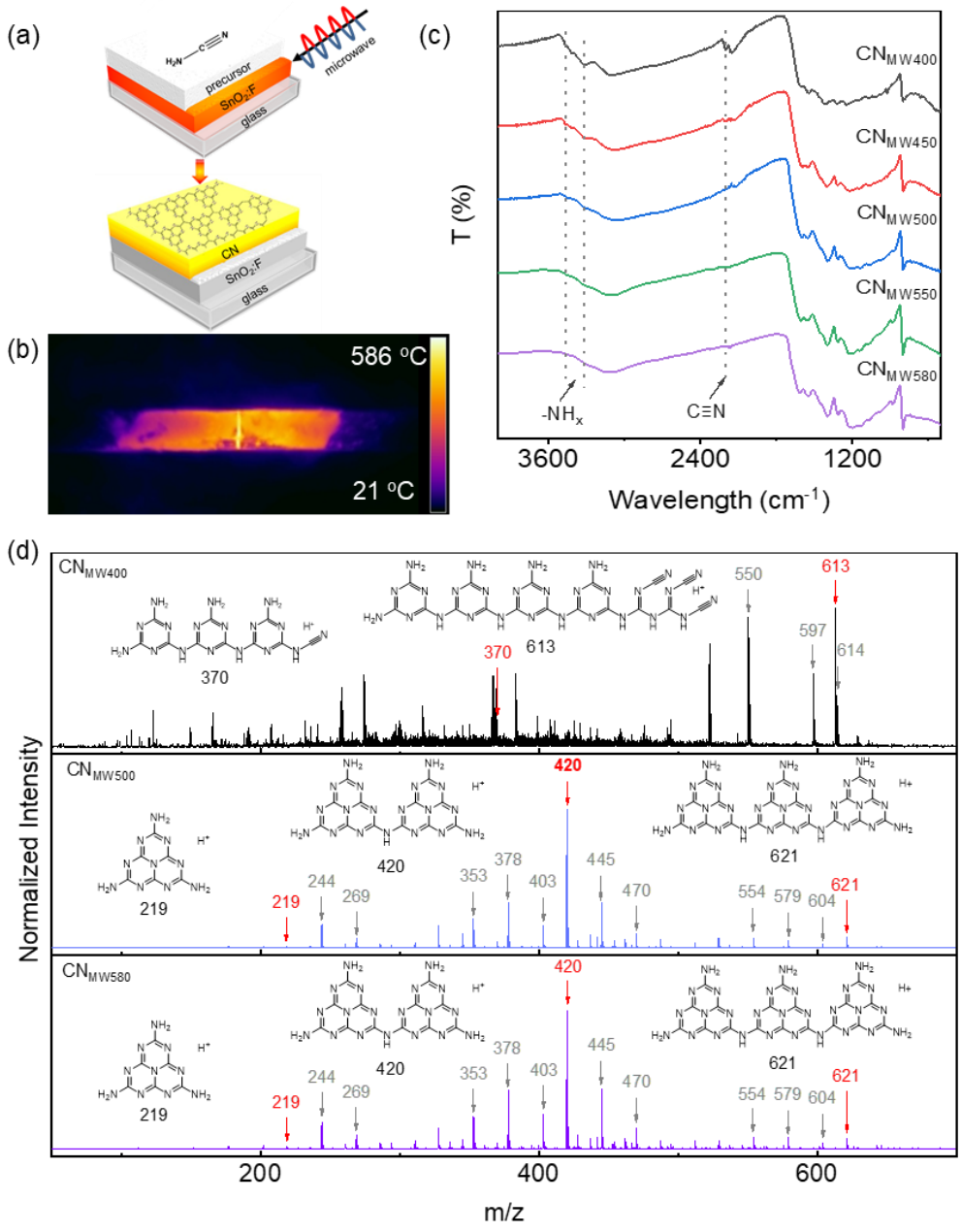

Figure 1. (a) Scheme of microwave-assisted synthesis of CN photoelectrode. (b) Thermal image for temperature distributions of CN_{MW580} on FTO by microwave heating. (c) FT-IR and (d) LDI-TOF mass spectra of CN_{MWT} (T= 400 to 580 °C)

To disclose more precise evolution of molecular structures, especially for the exact type of repeating units, during the condensation synthesis of CN_{MWT}, the matrix-free laser desorption/ionization time-of-flight (LDI-TOF) mass spectra of CN_{MW400}, CN_{MW500}, CN_{MW580} (**Figure 1d**) and the control bulk CN_{550} (**Figure S8**) were further measured. Interestingly, the m/z fragments of 370, 550, 597, 613, and 614 that were assignable to the linear oligomers of the triazine unit were observed for all samples (**Figure S9**). Nevertheless, the relative intensity gradually decreased when the condensation temperature was elevated. Moreover, the mass spectra of CN_{MW500} and CN_{MW580} showed 219, 420, and 621 m/z fragments, the same as that of bulk CN_{550}, with an interval of 201. It corresponded to the successive loss of protonated heptazine in ionization[35]. A series of peaks with m/z separated by 17, 42, 67, 151, 176, and 201 were also observed, showing the progressive ionization of heptazine to cyanamide (see more discussion in SI and **Table S1**). Besides, multiple LDI-TOF mass spectra measurements showed that the relative m/z fragment intensity of 621, assigning to heptazine trimer, successively increased during the polymerization, indicating an improved polymerization degree at a higher temperature. The by-products, including dicyandiamide, melamine, and melam during the synthesis of CN_{MW580}, were also identified by FTIR (**Figure S10a**), XRD patterns (**Figure S10b**), and high-performance liquid chromatography (HPLC)-mass spectrometry (**Figure S11**).

Given the above, the detailed thermal-condensation processes of CN_{MWT} were summarized as follows: (1) triazine repeating units with cyano-terminal groups were firstly produced from monomers; (2) they later converted into a more conjugated heptazine framework when the critical temperature (ca. 500 ºC) was reached; (3) at a higher temperature up to 580 ºC, the polymerization degree increased; (4) and finally, at an even higher temperature, CN_{MWT} started to decompose (**Figure S13**). Notably, our results showed that the triazine unit was always accompanied by the electron-drawing cyano-terminal groups during the condensation reaction, while the heptazine unit was not. It was supposed that such molecular structures evolution would alter the HOMO-

LUMO orbits delocalization of CN_{MWT} and subsequently influence the ECL efficiency, which will be discussed in the following text.

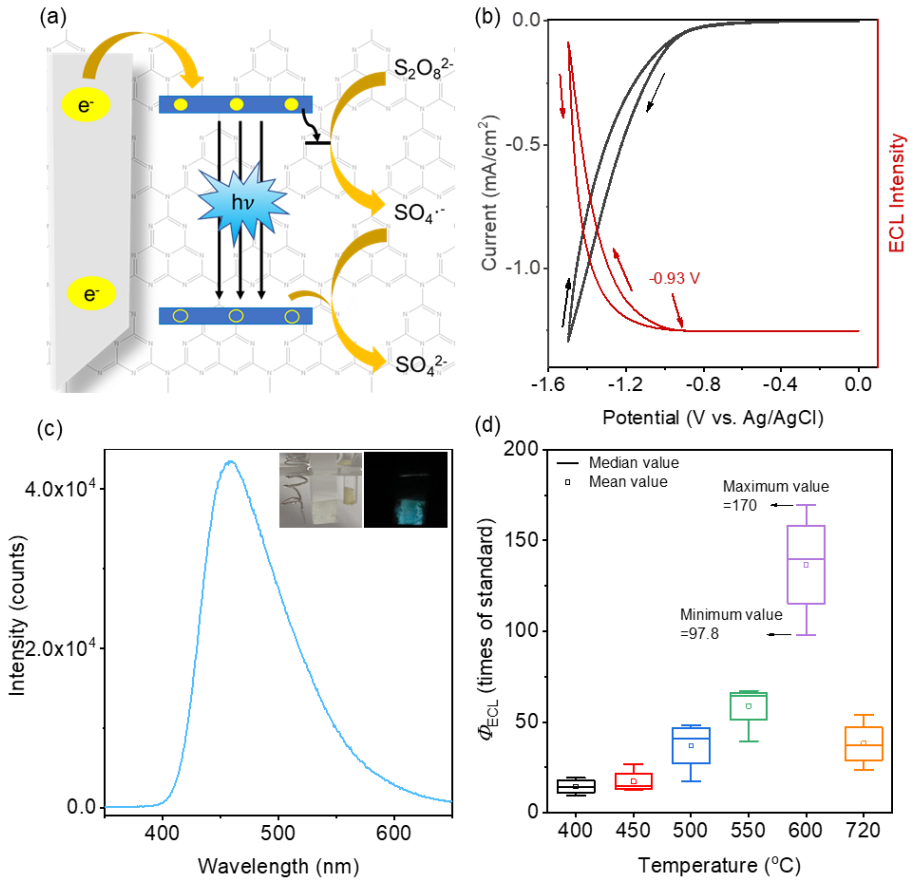

Figure 2. (a) Proposed ECL mechanism at CN_{MWT}. (b) CV and ECL curves of CN_{MW580}. (c) Wavelength-resolved ECL spectrum of CN_{MW580} under -1.5 V vs. Ag/AgCl that was used for calculating the total number of photons. Insets: the photographs of CN_{MW580} electrode before and after applying voltage in the daylight and dark. (d) The relative ECL efficiency of CN_{MWT}. Electrolyte: 0.01 M PBS, 0.1 M KCl and 25 mM $K_2S_2O_8$.

ECL is the emission of light produced by the electron transfer reaction between the electrochemically generated species in the vicinity of an electrode.[2, 36] **Figure 2a** shows that the entire ECL processes of CN can be divided into four steps. The first is the injection of electrons from the working electrode into CN's conduction band (CB). Next, partially excited electrons reduced the co-reagent, producing potent oxidant radicals. It

later initiated the third step, i.e., hole-generation in the valence band (VB). Lastly, the electrons in the CB and the holes in the VB recombine with the emission of lights.[37] The cyclic voltammogram (CV) curve showed the injection of electrons (**Step 1**) for CN_{MW580} at an onset potential of ca. -0.93 V; simultaneously, the ECL emission was observed (**Figure 2b**), even by naked eyes (**Figure 2c inset**). The wavelength-resolved ECL spectrum in **Figure 2c** demonstrated an intense peak centered at ca. 460 nm, almost identical to its optical bandgap (**Figure S7**), manifesting the above CB-VB transition mechanism[30].

Our previous microwave-assisted synthesis work obtained a historic record cathodic ECL efficiency of ca. seven times of benchmark $Ru(bpy)_3Cl_2$.[37] This study revealed that by optimizing the microwave sampling position (**Figure S14**), the heating temperature could be further substantially improved from prevenient 400 ºC to 720 ºC, fully covering the condensation and decomposition temperature for CN. Interestingly, as shown in **Figure 2d**, the relative ECL efficiency (Φ_{ECL}, **Eqn. 1**) demonstrated a volcano relationship with the synthesis temperature, and the highest one of CN_{MW580} reached a new milestone of 170 times of benchmark $Ru(bpy)_3Cl_2$ (see the detailed calculation in **Figure S15**). Thanks to the variable molecular structures discussed in the above section, CN_{MWT} offered a versatile platform to understand the intrinsic factors that influence Φ_{ECL}.

To verify how electrons participated in the ECL processes in **Step 1**, the electrochemical impedance spectra (EIS) and Mott−Schottky plots of different CN_{MWT} were measured. Generally, the semicircle diameter in Nyquist plots is equivalent to the electron-transfer resistance (R_p),[38] and low resistance favors electrons injection from substrate electrodes to emitters for cathodic ECL (**Step 1**). As shown in **Figure 3a and S16a**, the semicircle domain decreased with condensation temperature, indicating that the higher the condensation temperature, the higher the electron conductivity. Mott−Schottky plots under dark conditions were also analyzed. **Figure 3b** showed a lower slope for CN_{MWT} at high temperatures. As known, the slope of the Mott−Schottky plot was inversely correlated with the charge carrier density (**Eqn. 2**). It suggested that CN_{MWT} at higher

temperatures could improve the charge carrier density[39] (**Figure S16b**), which provided the origin of the enhanced electron conductivity of CN_{MWT}.

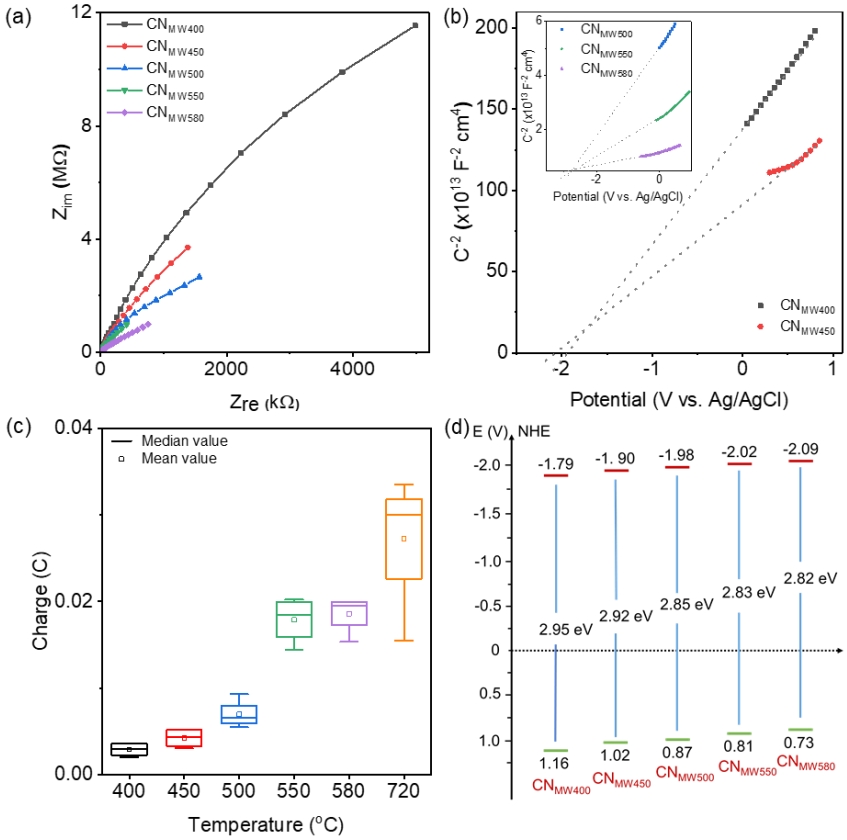

Figure 3. (a) Nyquist and (b) Mott−Schottky plots of different CN_{MWT} (T=400-580) in 0.1 M KCl. The inset shows the Mott−Schottky plots of CN_{MWT} (T=500-580) under same condition. (c) Charge consumed by Faraday reactions and (d) energy level diagram of different CN_{MWT} (T=400-580).

We next explored **Step 2 and 3**, in which $K_2S_2O_8$ co-reagent was successively reduced, followed by the generation of holes in the VB of CN_{MWT}. The ECL intensity-potential curves in **Figure S17** showed CN_{MWT} at higher temperature demonstrated a positively shifted ECL onset potential. As enabled by the formation of more heptazine units, the increased electronic conductivity of CN_{MWT} well supported the accelerated reduction of $K_2S_2O_8$ into $SO_4^{\bullet-}$ (**Step 2**). The charge consumed by Faraday reactions including $K_2S_2O_8$ and CN_{MWT} reduction could be quantitatively evaluated by

subtracting the consumed charge during chronoamperometric measurements in electrolyte without $K_2S_2O_8$ from that with $K_2S_2O_8$. As summarized in **Figure 3c**, the charge consumed by $K_2S_2O_8$ reduction in the ECL processes also increased for CN_{MWT} at high temperatures, which was supposed to generate more co-reagent radicals. To understand the formation of a hole in the VB of CN_{MWT}, the energy band structure of CN_{MWT} was further calculated by measuring the flat band potential using the onset of the photocurrent (**Figure S18**) and the band gap from the UV-vis absorption spectra (**Figure S8**). It was observed that the CB-VB position up-shifted with a shrinking gap for CN_{MWT} at a higher temperature. As such, the strong oxidizing species, i.e., $SO_4^{\bullet-}$, would be more easily generated and further extracted an electron from VB to produce a hole (**Step 3**). After this step, the excited CN_{MWT}* was formed. In these regards, the electronic conductivity and CB-VB position of CN_{MWT} at higher temperatures were more favorable to the kinetics of **Step 2 and 3** in the ECL for CN_{MWT}.

To understand the influencing factors for the photon dynamics in ECL (**Step 4**), the open-circuit photovoltage (OCP) was further measured. Generally, a larger OCP upon irradiation is often associated with solid excited electron storage. It was found that the OCP of all CN_{MWT} increased with time under the irradiation and gradually reached a plateau. Interestingly, the slopes (k_1) were higher for CN_{MWT} at a higher temperature, indicating faster electrochemical excitation kinetics **(Figure 4a)**, consistent with the lower ECL onset potential (**Figure S18**). A similar trend of the stabilized OCP under irradiation (ΔV_1) for all CN_{MWT} was also observed, indicating higher excited electron storage.[40-41] When the light was off, the OCP rapidly subsided. The slope, an indicator of the electron-hole recombination kinetics (k_2), was also higher for CN_{MWT} at higher temperatures. The surface deep electron-trapping state could be evaluated by the ratio of $\Delta V_2/\Delta V_1$ (α).[39, 42] It was observed that α of CN_{MWT} at higher temperature was closer to 1, suggesting less surface deep electron-trapping state. For clarity, the value of ΔV_1, Δ_2, k_1, and k_2 for different CN_{MWT} are summarized in **Figure S19**. Thus, the OCP measurement disclosed that CN_{MWT} at higher temperatures had higher excited electron-

storage capacity, favorable excitation, faster electron-hole recombination kinetics, and less surface deep trapping state of electrons.

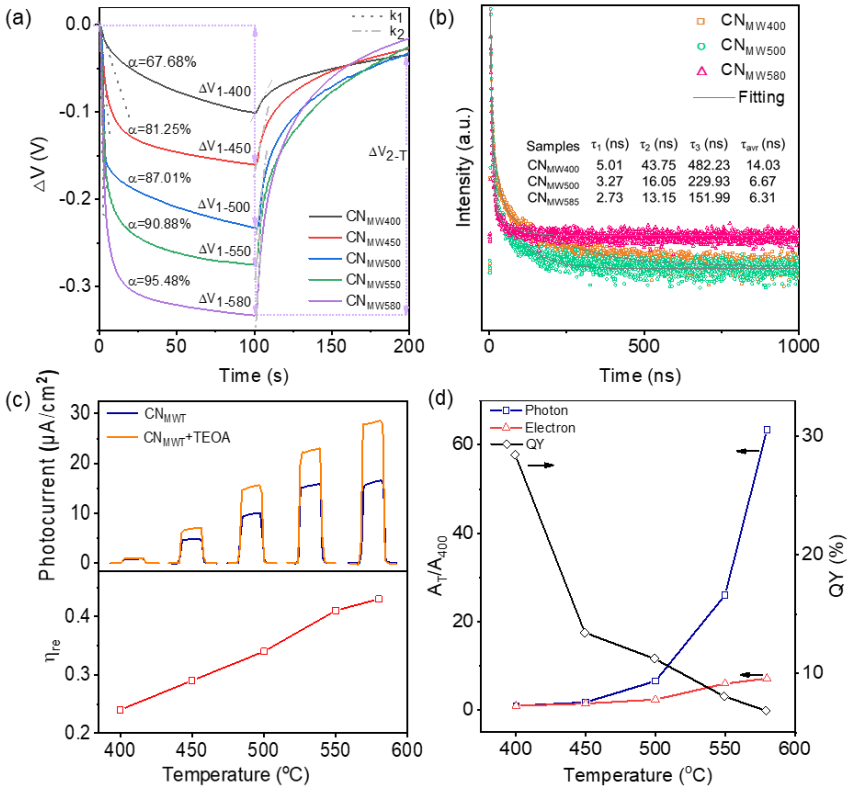

Figure 4. (a) Open circuit potential of different CN_{MWT} (T=400-580) under chopped visible light irradiation in 0.1 M KCl. (b) Time-resolved PL decay spectra and (c) holes recombination efficiency of CN_{MWT} (T=400-580) evaluated by PEC current under chopped light biased at -0.3 V vs. Ag/AgCl in 0.1 M KCl. (d) PL quantum yields, the number of emitted photons and the number of consumed electrons involved in the ECL of CN_{MWT} (T=400-580).

To confirm the above photon dynamics, the excited state of CN_{MWT} was also studied using the time-resolved PL decay spectra (**Figure 4b**), thanks to the similar CB-VB transition in ECL and PL. Three different processes contribute to the lifetime: the non-radiative process (τ_1), radiative process (τ_2), and energy transfer process (τ_3).[43-44] Among them, τ_2 is directly related to the recombination of photogenerated electron-

hole pairs,[43, 45] which was calculated to be 43.75, 16.05, and 13.15 ns for CN_{MWT} (T=400, 500 and 580), respectively. In general, a shorter PL decay lifetime of the radiative process often indicates a faster recombination rate for electron-hole pairs,[46] while an elongated one would result from the accumulation of excited electrons in the deep trapping state. To support this hypothesis for CN_{MWT}, triethanolamine (TEOA), an efficient hole scavenger, was added to the electrolytes. Assuming that most holes are successfully extracted in the system, the normalized photocurrent after the addition of TEOA could be set as 100%.[47-48] Based on this speculation, the calculated electron-hole recombination efficiency (η_{re}, **Eqn. 4**) of CN_{MWT} at higher temperature was higher (**Figure 4c, S20**), supporting the as-observed shorter PL decay lifetime and consistent with the OCP results (**Figure 4a**). Similarly, the R_p by EIS plots (**Figure S21a and b**) and the charge carrier density by Mott−Schottky plots (**Figure S21b and c**) under irradiation for CN_{MWT} also showed the consistent dependence on the condensation temperature. For instance, the charge carrier density of CN_{MW580} was quantitatively nearly 120 times that of CN_{MW400} under irradiation, showing the critical role of condensation temperature in enhancing the photon dynamics process.

The above results revealed that higher condensation temperature favored both the electron transfer and radiative process. Nonetheless, the detailed dependences were different. As shown in **Figure 4d**, the turnaround temperature for consumed electrons and emitted photons was observed both at ca. 500 °C, but beyond which, the former gradually reached a plateau, while the latter sharply boosted up to 580 °C. It should be noted that 500 and 580 °C were the critical temperatures for transforming triazine into heptazine and the decomposition of CN, respectively. According to the definition of Φ_{ECL}, it suggested that in the stable scope of carbon nitrides, the higher ratio of heptazine units, the higher Φ_{ECL}. In contrast, the PL quantum yields (QY) of the CN_{MWT} demonstrated a different dependence on the core repeating units (**Figure 4d**), indicating a distinctive mechanism.

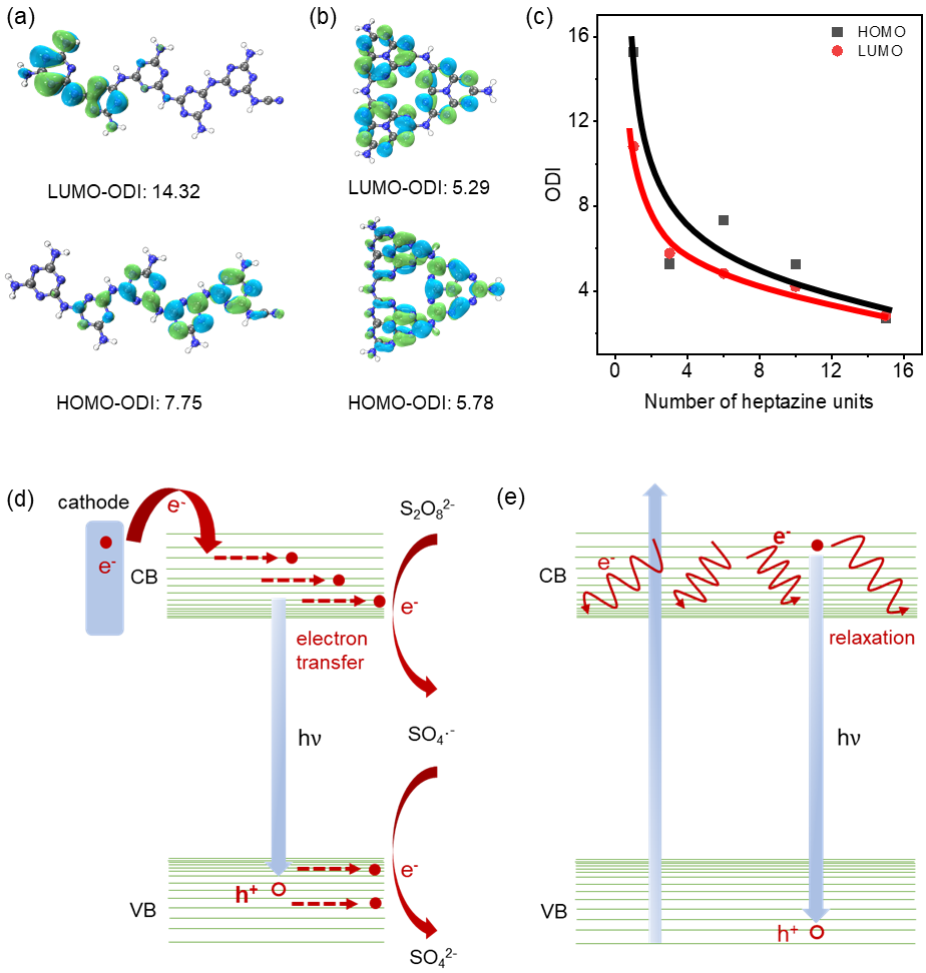

Figure 5. Isosurfaces of the LUMO (top) and HOMO (bottom) of the representative molecular structures of (a) CN_{MW400} and (b) CN_{MW580} along with the orbital delocalization index. (c) Plot of ODI for HOMO-LUMO with the different number of heptazine rings. Scheme of the proposed charge transfer in (d) ECL and (e) PL of CN_{MWT}.

In general, the ECL kinetics, such as electronic conductivity, excited electron-storage capacity, surface deep electron-trapping state, charge carrier density, and electron-hole recombination efficiency, were are all associated with the electronic structure of luminophores, for which, the orbital delocalization is supposed to be a practical desciptor.[49-51] To get more insights into the improved Φ_{ECL} for CN_{MWT}, the orbital delocalization index (ODI) of HOMO-LUMO for the typical fragments during the

successive thermal condensation of CN were quantitatively calculated by using DFT methods.[52] The ODI_i is defined as $0.01 \times \sum_A \Theta_{A,i}{}^2$, where $\Theta_{A,i}$ is the contribution degree of A atom for the i obit. The lower ODI in value, the higher the orbital delocalization. In addition, the ODI range is (0, 100]. It was found that due to the lone pair electrons, cyano-terminal groups, which always accompanied the generation of trazine during the condensation below the critical temperature of 400 ºC, mostly predominated the contribution for the HOMO and LUMO of CN_{MWT} (**Figure 5a**), manifesting a higher ODI. In contrast, the ODI of HOMO and LUMO for CN_{MWT} with heptazine framework decreased (**Figure 5b**) and became even lower with a higher polymerization degree (**Figure 5c**), indicating electrons were ready to transfer in a more polymerized structure. Such significant ODI changes for different CN fragments supported the experimental observation that CN_{MWT} at higher temperatures had favorable electron injection in dark and photon emission afterward. Therefore, during the thermal condensation of CN, the structure transformation regarding the terminal groups and triazine/heptazine core frameworks was essentially associated with a gradual improvement in the orbital delocalization. Factoring out the complicated structure evolution, ODI could be regarded as a unified intrinsic factor for Φ_{ECL} of CN, i.e., the lower ODI, the higher Φ_{ECL}.

For clarity, the possible charge-transfer pathway for ECL (**Figure 5c**) and PL (**Figure 5d**) of CN_{MWT} was briefly proposed**.** Due to the unique electrochemical excitation, an efficient obits delocalization would promote electron injection and co-reagent reduction reaction kinetics. In contrast, the same situation was often associated with non-radiative decay pathways for photoexcitation, leading to a PL quenching. Understanding the effects of electron delocalization on the unique electrochemical excitation and light emission for ECL would unlock the intrinsic factors for boosting Φ_{ECL}. As a result, owing to the enhanced HOMO and LUMO delocalization, the as-synthesized CN_{MW580} demonstrated the highest Φ_{ECL} in this work, reaching a new milestone of 134-fold greater than the benchmark $Ru(bpy)_3Cl_2$ (**Figure 2d**). Moreover, taking detection of $NaNO_2$ as an example application, a near tenfold larger slope of the calibration curve

was obtained by using CN_{MW580}, compared to CN_{MW400} (**Figure S22**). It evidently suggested that CN_{MWT} with higher Φ_{ECL} held great potentials in developing chemical sensors with superior sensitivity.

Conclusion

In summary, we report that the orbital delocalization of CN was a practically unifying factor for its ECL efficiency. The comprehensive characterizations, including LDI-TOF mass spectroscopy, confirmed the critical molecular transformation from triazine to heptazine basal frameworks at 500 ºC, accompanying the disappearance of cyano-terminal groups. Apart from PL property in previous studies, each electron- and photon-participated process in ECL of CN was further systematically explored to examine the ECL kinetics, such as electronic conductivity, excited electron-storage capacity, surface deep electron-trapping state, charge carrier density, and electron-hole recombination efficiency. The resulting DFT calculation disclosed the intrinsic correlation between molecular structure and ECL kinetics, i.e., behind the complicated molecular structure evolution, the orbital delocalization of CN was essentially improved at successive elevated condensation temperature, which favored the electron injection in excitation and photon emission afterward in ECL. As a result, interestingly, the cathodic Φ_{ECL} of CN calcining at 580 ºC before the decomposition was remarkably improved to a new milestone up to ca. 170-fold greater than that of benchmark $Ru(bpy)_3Cl_2$.This work demonstrates that a better understanding of intrinsic factors, such as the orbital delocalization for CN, is promising to unlock luminophores with higher Φ_{ECL} and pave more demanding applications.

Experimental Procedures

Reagent. Cyanamide (CA, 99%) was purchased from Energy Chemical, China. Potassium peroxodisulfate ($K_2S_2O_8$), potassium chloride (KCl), sodium dihydrogen phosphate dihydrate ($NaH_2PO_4{\cdot}2H_2O$), disodium hydrogen phosphate dodecahydrate ($Na_2HPO_4{\cdot}12H_2O$), triethanolamine (TEOA) and sodium nitrite ($NaNO_2$) were obtained

from Shanghai Macklin Biochemical Co. Ltd., China. Fluorine-doped tin oxide (FTO) glasses (12-14 Ω/sq, Zhuhai Kaivo Optoelectronic Technology Co., Ltd., China) was ultrasonically washed with acetone, alcohol, and ultrapure water for 15 min, respectively, and then dried with high pure nitrogen gas flow before use. Ultrapure water (18.2 MΩ·cm) was obtained from a Direct-Q 3 UV pure water purification system (Millipore, USA) throughout all experiments. Unless otherwise specified, all the other reagents were of analytical grade and applied without further purification.

Characterization. Fourier transformed infrared spectra (FT-IR) were recorded using Nicolet iS10 FT-IR spectrometer, equipped with an attenuated total reflection (ATR) setup (Thermo, USA). The structure of CN_{MWT} was obtained by matrix-free laser desorption/ionization time-of-flight mass (LDI-TOF-MS, AB Sciex 5800, America). The morphology of the CN_{MWT} electrode were investigated by FEI Inspect F50 scanning electron microscope (FEI, USA). The XRD patterns were measured by using Ultima IV (Rigaku, Japan). X-ray photoelectron spectroscopy (XPS) was taken on an ESCALAB 250XI electron spectrometer (Thermo, USA) with monochromatic Al Kα X-rays (hν = 1486.6 eV) as the excitation source, and the binding energy were corrected by reference C1s level to 284.6 eV to compensate for the specimen charging. The UV-vis absorption spectra were measured on a Cary 100 (Agilent, Singapore) with a diffuse-reflectance accessory, and $BaSO_4$ was used as a standard reference (100% reflectance). The photoluminescence (PL) spectra were performed on a Fluoromax-4 (Horiba Jobin Yvon, Japan). The time-resolved PL spectra were performed with fluorescence spectrometer (PluoroLog 3-TCSPC, Horiba Jobin Yvon, Japan). The high-performance liquid chromatography (HPLC, Agilent, 1260-Infifinity) at a detection wavelength of 230 nm with a methanol/water mixture (80:20, v/v) as the mobile phase. Thermal gravimetric analysis (TGA) was performed using a (TG209 F3, Netzsch, Germany) analyzer with a heating rate of 10 ºC/min from 25 ºC to 800 ºC under a nitrogen atmosphere.

Preparation of CN photoelectrode. Firstly, CA was heated at 80 ºC and melted. Then, 30 μL of CA was dropped on the conductive side of FTO. After that, the microwave

oven (M1-L213B, 2.45 GHz, Midea, China) were used to heat CA using FTO as microwave interaction agent operating with the power of 700 W and cooled to room temperature naturally. The thermal imaging device (AnalyzIR FOTRIC 280, China) were used for monitoring the CN_{MW} synthesis process. A microwave leakage detector (DT-2G, CEM, China) was used to monitor external field intensities around the oven in order to safety precaution.

ECL Measurements. The ECL intensity measurements were conducted on an ECL analyzer system (MPI-E, Xi'an Ruimai Analytical Instruments Co. Ltd., China). The voltage of photomultiplier tube (PMT) for collecting the ECL signal was biased at 400 V during detection. The supporting electrolyte was 0.1 M KCl with 25 mM $K_2S_2O_8$ in 0.01 M PBS (pH 7.4).[31, 53] The ECL emission spectra were recorded by integrating CHI 400C with an Fluoromax-4 FL spectrophotometer, where the slit width was 20 nm.

Relative ECL efficiency (Φ_{ECL}). Φ_{ECL} are defined as the ratio of the number of photons produced per electron transferred between the oxidized and reduced analyte species relative to that of $Ru(bpy)_3Cl_2/K_2S_2O_8$, using **Eqn. 1**:[53-54]

$$\phi_{ECL} = \frac{\left(\frac{\int ECL\, dt}{\int \text{Current dt}}\right)x}{\left(\frac{\int ECL\, dt}{\int Current\, dt}\right)st} \times 100\% \qquad (1)$$

where "*ECL*" and "*Current*" represent integrated ECL intensity from the accumulated ECL spectrum and electrochemical current values respectively, "*st*" refers to the $Ru(bpy)_3Cl_2/K_2S_2O_8$ standard and "*x*" refers to the analyte. The potential was fixed at -1.5 V vs. Ag/AgCl by chronoamperometry in 0.01 M PBS (pH 7.4) containing 25 mM $K_2S_2O_8$ and 0.1 M KCl.

Photoelectrochemical measurements. All the electrochemical measurements were performed with a conventional three-electrode system, consisting of CN_{MWT} on FTO electrode, platinum wires, Ag/AgCl in saturated KCl as working electrode, counter electrode, and reference electrode, respectively. The PEC experiments were measured out in 0.1 M KCl at ambient condition. The light source to simulate the sunlight was obtained from a 150 W Xe lamp and the average light intensity was 100 mW/cm^2.The

electrochemical impedance spectroscopy (EIS), open circus potential (OCP) and Mott-Schottky plots were recorded in a Reference 600 potentiostat/galvanostat/ZRA (Gamry, USA). The potentials were measured against the Ag/AgCl (saturated KCl). The working electrode was irradiated from the backside in order to minimize the influence of thickness of the semiconductor layer. The Mott-Schottky equation (**Eqn. 2**) simply relates C to the applied potential V relative to its V_{fb} and other parameters of the semiconductor as follows:[39, 55]

$$\frac{1}{C^2} = \frac{2}{\varepsilon\varepsilon_{0A^2eN_D}}\left(V - V_{fb} - \frac{k_BT}{e}\right) \quad (2)$$

$$Slope = \frac{2}{\varepsilon\varepsilon_{0A^2eN_D}} \quad (3)$$

where ε and ε_0 are the dielectric constant and the vacuum permittivity, respectively, A is the area, e is the electronic charge, V_{fb} is the flat-band potential, N_D and the donor concentration, (for an n-type semiconductor photoanode), or acceptor concentration, V is applied potential, k_B is the Boltzmann constant, and T is the temperature. The N_D is proportional to the inverse of the slope.

Hole recombination efficiency. The hole recombination efficiency was calculated using **Eqn. 4**:[47, 56]

$$\eta_{re}(\%) = 1 - \frac{J_{KCl}}{J_{TEOA}} \times 100\% \quad (4)$$

It is assumed that the recombination efficiency of photogenerated carriers in the system is 100% after the addition of a hole scavenger (10% v/v TEOA). J_{KCl} is the photocurrent density obtained in 0.1 M KCl aqueous solution, while J_{TEOA} is the photocurrent density obtained in 0.1 M KCl containing 10% (v/v) TEOA.

Computational methods. Density functional theory (DFT) calculations were performed with Gaussian 16 (revision A03).[57] The models were optimized at the M06-2X/6-311g(d,p) level without imaginary frequency. The ODI was calculated by Multiwfn (revision 3.8).[58] The images of isosurfaces of the LUMO and HOMO were obtained from Visual Molecular Dynamics (VMD, revision 1.9.3) and Multiwfn (revision 3.8).

Reference

1. Pan, D.; Fang, Z.; Yang, E.; Ning, Z.; Zhou, Q.; Chen, K.; Zheng, Y.; Zhang, Y.; Shen, Y., Facile Preparation of WO_{3-x} Dots with Remarkably Low Toxicity and Uncompromised Activity as Co-reactants for Clinical Diagnosis by Electrochemiluminescence. *Angew. Chem. Int. Ed.* **2020,** *59*, 16747-16754.
2. Voci, S.; Goudeau, B.; Valenti, G.; Lesch, A.; Jović, M.; Rapino, S.; Paolucci, F.; Arbault, S.; Sojic, N., Surface-Confined Electrochemiluminescence Microscopy of Cell Membranes. *J. Am. Chem. Soc.* **2018,** *140*, 14753-14760.
3. Zhang, J.; Jin, R.; Jiang, D.; Chen, H.-Y., Electrochemiluminescence-Based Capacitance Microscopy for Label-Free Imaging of Antigens on the Cellular Plasma Membrane. *J. Am. Chem. Soc.* **2019,** *141*, 10294-10299.
4. Yang, Y.; Yao, L.-Y.; Liang, W.-B.; Huang, W.; Zhang, Y.-J.; Zhang, J.-L.; Yuan, R.; Xiao, D.-R., Highly efficient electrochemiluminescence resonance energy transfer material constructed from an AIEgen-based 2D ultrathin metal–organic layer for thrombin detection. *Chem. Commun.* **2021,** *57*, 4323-4326.
5. Zhou, X.; Zhu, D.; Liao, Y.; Liu, W.; Liu, H.; Ma, Z.; Xing, D., Synthesis, labeling and bioanalytical applications of a tris(2,2′-bipyridyl)ruthenium(II)-based electrochemiluminescence probe. *Nat. Protoc.* **2014,** *9*, 1146-1159.
6. Zanut, A.; Fiorani, A.; Canola, S.; Saito, T.; Ziebart, N.; Rapino, S.; Rebeccani, S.; Barbon, A.; Irie, T.; Josel, H.-P.; Negri, F.; Marcaccio, M.; Windfuhr, M.; Imai, K.; Valenti, G.; Paolucci, F., Insights into the mechanism of coreactant electrochemiluminescence facilitating enhanced bioanalytical performance. *Nat. Commun.* **2020,** *11*, 1-9.
7. Chen, A.; Liang, W.; Wang, H.; Zhuo, Y.; Chai, Y.; Yuan, R., Anodic Electrochemiluminescence of Carbon Dots Promoted by Nitrogen Doping and Application to Rapid Cancer Cell Detection. *Anal. Chem.* **2019,** *92*, 1379-1385.
8. Rubinstein, I.; Bard, A. J., Electrogenerated chemiluminescence. 37. Aqueous ecl systems based on tris(2,2'-bipyridine)ruthenium$_3^{2+}$ and oxalate or organic acids. *J. Am. Chem. Soc.* **2002,** *103*, 512-516.
9. Ishimatsu, R.; Matsunami, S.; Kasahara, T.; Mizuno, J.; Edura, T.; Adachi, C.; Nakano, K.; Imato, T., Electrogenerated Chemiluminescence of Donor-Acceptor Molecules with Thermally Activated Delayed Fluorescence. *Angew. Chem. Int. Ed.* **2014,** *126*, 7113-7116.
10. Zhang, R.; Tong, F.; Yang, L.; Adsetts, J. R.; Yan, T.; Wang, R.; Ding, Z.; Wang, H.-B., Facile synthesis and efficient electrochemiluminescence of a readily accessible pyridopyrimidine. *Chem. Commun.* **2018,** *54*, 9897-9900.
11. Cao, Z.; Shu, Y.; Qin, H.; Su, B.; Peng, X., Quantum Dots with Highly Efficient, Stable, and Multicolor Electrochemiluminescence. *ACS Cent. Sci.* **2020,** *6*, 1129-1137.
12. Chen, S.; Ma, H.; Padelford, J. W.; Qinchen, W.; Yu, W.; Wang, S.; Zhu, M.; Wang, G., Near Infrared Electrochemiluminescence of Rod-Shape 25-Atom AuAg Nanoclusters That Is Hundreds-Fold Stronger Than That of $Ru(bpy)_3$ Standard. *J. Am. Chem. Soc.* **2019,** *141*, 9603-9609.
13. Carrara, S.; Aliprandi, A.; Hogan, C. F.; De Cola, L., Aggregation-Induced

Electrochemiluminescence of Platinum(II) Complexes. *J. Am. Chem. Soc.* **2017,** *139*, 14605-14610.
14. Han, Z.; Zhang, Y.; Wu, Y.; Li, Z.; Bai, L.; Huo, S.; Lu, X., Substituent-Induced Aggregated State Electrochemiluminescence of Tetraphenylethene Derivatives. *Anal. Chem.* **2019,** *91*, 8676-8682.
15. Wang, N.; Gao, H.; Li, Y.; Li, G.; Chen, W.; Jin, Z.; Lei, J.; Wei, Q.; Ju, H., Dual Intramolecular Electron Transfer for In Situ Coreactant-Embedded Electrochemiluminescence Microimaging of Membrane Protein. *Angew. Chem. Int. Ed.* **2020,** *60*, 197-201.
16. Swanick, K. N.; Ladouceur, S.; Zysman-Colman, E.; Ding, Z., Self-Enhanced Electrochemiluminescence of an Iridium(III) Complex: Mechanistic Insight. *Angew. Chem. Int. Ed.* **2012,** *124*, 11241-11244.
17. Booker, C.; Wang, X.; Haroun, S.; Zhou, J.; Jennings, M.; Pagenkopf, B. L.; Ding, Z., Tuning of Electrogenerated Silole Chemiluminescence. *Angew. Chem. Int. Ed.* **2008,** *47*, 7731-7735.
18. Oh, J.-W.; Lee, Y. O.; Kim, T. H.; Ko, K. C.; Lee, J. Y.; Kim, H.; Kim, J. S., Enhancement of Electrogenerated Chemiluminescence and Radical Stability by Peripheral Multidonors on Alkynylpyrene Derivatives. *Angew. Chem. Int. Ed.* **2009,** *48*, 2522-2524.
19. Jiang, D.; Du, X.; Liu, Q.; Hao, N.; Qian, J.; Dai, L.; Mao, H.; Wang, K., Anchoring AgBr nanoparticles on nitrogen-doped graphene for enhancement of electrochemiluminescence and radical stability. *Chem. Commun.* **2015,** *51*, 4451-4454.
20. Hesari, M.; Lu, J.-s.; Wang, S.; Ding, Z., Efficient electrochemiluminescence of a boron-dipyrromethene (BODIPY) dye. *Chem. Commun.* **2015,** *51*, 1081-1084.
21. Wei, X.; Zhu, M. J.; Cheng, Z.; Lee, M.; Yan, H.; Lu, C.; Xu, J. J., Aggregation-Induced Electrochemiluminescence of Carboranyl Carbazoles in Aqueous Media. *Angew. Chem. Int. Ed.* **2019,** *58*, 3162-3166.
22. Peng, H.; Huang, Z.; Deng, H.; Wu, W.; Huang, K.; Li, Z.; Chen, W.; Liu, J., Dual Enhancement of Gold Nanocluster Electrochemiluminescence: Electrocatalytic Excitation and Aggregation-Induced Emission. *Angew. Chem. Int. Ed.* **2019,** *59*, 9982-9985.
23. Adsetts, J. R.; Hoesterey, S.; Gao, C.; Love, D. A.; Ding, Z., Electrochemiluminescence and Photoluminescence of Carbon Quantum Dots Controlled by Aggregation-Induced Emission, Aggregation-Caused Quenching, and Interfacial Reactions. *Langmuir* **2020,** *36*, 14432-14442.
24. Han, Z.; Yang, Z.; Sun, H.; Xu, Y.; Ma, X.; Shan, D.; Chen, J.; Huo, S.; Zhang, Z.; Du, P.; Lu, X., Electrochemiluminescence Platforms Based on Small Water-Insoluble Organic Molecules for Ultrasensitive Aqueous-Phase Detection. *Angew. Chem. Int. Ed.* **2019,** *58*, 5915-5919.
25. Liu, X.; Shi, L.; Niu, W.; Li, H.; Xu, G., Environmentally Friendly and Highly Sensitive Ruthenium(II) Tris(2,2′-bipyridyl) Electrochemiluminescent System Using 2-(Dibutylamino)ethanol as Co-Reactant. *Angew. Chem. Int. Ed.* **2007,** *46*, 421-424.
26. Lv, Y.; Chen, S.; Shen, Y.; Ji, J.; Zhou, Q.; Liu, S.; Zhang, Y., Competitive Multiple-Mechanism-Driven Electrochemiluminescent Detection of 8-Hydroxy-2′-

deoxyguanosine. *J. Am. Chem. Soc.* **2018,** *140*, 2801-2804.
27. Ji, J.; Wen, J.; Shen, Y.; Lv, Y.; Chen, Y.; Liu, S.; Ma, H.; Zhang, Y., Simultaneous Noncovalent Modification and Exfoliation of 2D Carbon Nitride for Enhanced Electrochemiluminescent Biosensing. *J. Am. Chem. Soc.* **2017,** *139*, 11698-11701.
28. Feng, Q.-M.; Shen, Y.-Z.; Li, M.-X.; Zhang, Z.-L.; Zhao, W.; Xu, J.-J.; Chen, H.-Y., Dual-Wavelength Electrochemiluminescence Ratiometry Based on Resonance Energy Transfer between Au Nanoparticles Functionalized g-C_3N_4 Nanosheet and $Ru(bpy)_3^{2+}$ for microRNA Detection. *Anal. Chem.* **2015,** *88*, 937-944.
29. Zou, R.; Lin, Y.; Lu, C., Nitrogen Vacancy Engineering in Graphitic Carbon Nitride for Strong, Stable, and Wavelength Tunable Electrochemiluminescence Emissions. *Anal. Chem.* **2021,** *93*, 2678-2686.
30. Zhao, T.; Zhou, Q.; Lv, Y.; Han, D.; Wu, K.; Zhao, L.; Shen, Y.; Liu, S.; Zhang, Y., Ultrafast Condensation of Carbon Nitride on Electrodes with Exceptional Boosted Photocurrent and Electrochemiluminescence. *Angew. Chem. Int. Ed.* **2019,** *59*, 1139-1143.
31. Zhou, Z.; Shang, Q.; Shen, Y.; Zhang, L.; Zhang, Y.; Lv, Y.; Li, Y.; Liu, S.; Zhang, Y., Chemically Modulated Carbon Nitride Nanosheets for Highly Selective Electrochemiluminescent Detection of Multiple Metal-ions. *Anal. Chem.* **2016,** *88*, 6004-6010.
32. Zhou, Z.; Wang, J.; Yu, J.; Shen, Y.; Li, Y.; Liu, A.; Liu, S.; Zhang, Y., Dissolution and Liquid Crystals Phase of 2D Polymeric Carbon Nitride. *J. Am. Chem. Soc.* **2015,** *137*, 2179-2182.
33. Huang, C.; Wen, Y.; Ma, J.; Dong, D.; Shen, Y.; Liu, S.; Ma, H.; Zhang, Y., Unraveling fundamental active units in carbon nitride for photocatalytic oxidation reactions. *Nat. Commun.* **2021,** *12*, 320.
34. Wang, W.; Zhang, H.; Zhang, S.; Liu, Y.; Wang, G.; Sun, C.; Zhao, H., Potassium-Ion-Assisted Regeneration of Active Cyano Groups in Carbon Nitride Nanoribbons: Visible-Light-Driven Photocatalytic Nitrogen Reduction. *Angew. Chem. Int. Ed.* **2019,** *58*, 16644-16650.
35. Lau, V. W.-h.; Mesch, M. B.; Duppel, V.; Blum, V.; Senker, J.; Lotsch, B. V., Low-Molecular-Weight Carbon Nitrides for Solar Hydrogen Evolution. *J. Am. Chem. Soc.* **2015,** *137*, 1064-1072.
36. Valenti, G.; Scarabino, S.; Goudeau, B.; Lesch, A.; Jović, M.; Villani, E.; Sentic, M.; Rapino, S.; Arbault, S.; Paolucci, F.; Sojic, N., Single Cell Electrochemiluminescence Imaging: From the Proof-of-Concept to Disposable Device-Based Analysis. *J. Am. Chem. Soc.* **2017,** *139*, 16830-16837.
37. Zhao, T.; Zhou, Q.; Lv, Y.; Han, D.; Wu, K.; Zhao, L.; Shen, Y.; Liu, S.; Zhang, Y., Ultrafast Condensation of Carbon Nitride on Electrodes with Exceptional Boosted Photocurrent and Electrochemiluminescence. *Angew. Chem. Int. Ed.* **2019**, 1139-1143.
38. Jiang, W.; Zhao, Y.; Zong, X.; Nie, H.; Niu, L.; An, L.; Qu, D.; Wang, X.; Kang, Z.; Sun, Z., Photocatalyst for High-Performance H_2 Production: Ga-Doped Polymeric Carbon Nitride. *Angew. Chem. Int. Ed.* **2021,** *60*, 6124-6129.
39. Ruan, Q.; Miao, T.; Wang, H.; Tang, J., Insight on Shallow Trap States-Introduced Photocathodic Performance in n-Type Polymer Photocatalysts. *J. Am. Chem. Soc.* **2020,**

142, 2795-2802.
40. Lau, V. W.-h.; Klose, D.; Kasap, H.; Podjaski, F.; Pignié, M.-C.; Reisner, E.; Jeschke, G.; Lotsch, B. V., Dark Photocatalysis: Storage of Solar Energy in Carbon Nitride for Time-Delayed Hydrogen Generation. *Angew. Chem. Int. Ed.* **2017,** *56*, 510-514.
41. Che, W.; Cheng, W.; Yao, T.; Tang, F.; Liu, W.; Su, H.; Huang, Y.; Liu, Q.; Liu, J.; Hu, F.; Pan, Z.; Sun, Z.; Wei, S., Fast Photoelectron Transfer in (Cring)–C_3N_4 Plane Heterostructural Nanosheets for Overall Water Splitting. *J. Am. Chem. Soc.* **2017,** *139*, 3021-3026.
42. Ruan, Q.; Bayazit, M. K.; Kiran, V.; Xie, J.; Wang, Y.; Tang, J., Key factors affecting photoelectrochemical performance of g-C_3N_4 polymer films. *Chem. Commun.* **2019,** *55*, 7191-7194.
43. Huang, Y.; Wang, Y.; Bi, Y.; Jin, J.; Ehsan, M. F.; Fu, M.; He, T., Preparation of 2D hydroxyl-rich carbon nitride nanosheets for photocatalytic reduction of CO_2. *RSC Adv.* **2015,** *5*, 33254-33261.
44. Niu, P.; Zhang, L.; Liu, G.; Cheng, H.-M., Graphene-Like Carbon Nitride Nanosheets for Improved Photocatalytic Activities. *Adv. Funct. Mater.* **2012,** *22*, 4763-4770.
45. Elbanna, O.; Fujitsuka, M.; Majima, T., g-C_3N_4/TiO_2 Mesocrystals Composite for H_2 Evolution under Visible-Light Irradiation and Its Charge Carrier Dynamics. *ACS Appl. Mater. Inter.* **2017,** *9*, 34844-34854.
46. Jiang, Q.; Zhao, Y.; Zhang, X.; Yang, X.; Chen, Y.; Chu, Z.; Ye, Q.; Li, X.; Yin, Z.; You, J., Surface passivation of perovskite film for efficient solar cells. *Nat. Photon.* **2019,** *13*, 460-466.
47. Qin, J.; Barrio, J.; Peng, G.; Tzadikov, J.; Abisdris, L.; Volokh, M.; Shalom, M., Direct growth of uniform carbon nitride layers with extended optical absorption towards efficient water-splitting photoanodes. *Nat. Commun.* **2020,** *11*, 4701.
48. Peng, G.; Albero, J.; Garcia, H.; Shalom, M., A Water-Splitting Carbon Nitride Photoelectrochemical Cell with Efficient Charge Separation and Remarkably Low Onset Potential. *Angew. Chem. Int. Ed.* **2018,** *130*, 16033-16037.
49. Ziebel, M. E.; Darago, L. E.; Long, J. R., Control of Electronic Structure and Conductivity in Two-Dimensional Metal–Semiquinoid Frameworks of Titanium, Vanadium, and Chromium. *J. Am. Chem. Soc.* **2018,** *140*, 3040-3051.
50. Che, Y.; Datar, A.; Yang, X.; Naddo, T.; Zhao, J.; Zang, L., Enhancing One-Dimensional Charge Transport through Intermolecular π-Electron Delocalization: Conductivity Improvement for Organic Nanobelts. *J. Am. Chem. Soc.* **2007,** *129*, 6354-6355.
51. Crispin, X.; Cornil, J.; Friedlein, R.; Okudaira, K. K.; Lemaur, V.; Crispin, A.; Kestemont, G.; Lehmann, M.; Fahlman, M.; Lazzaroni, R.; Geerts, Y.; Wendin, G.; Ueno, N.; Brédas, J.-L.; Salaneck, W. R., Electronic Delocalization in Discotic Liquid Crystals: A Joint Experimental and Theoretical Study. *J. Am. Chem. Soc.* **2004,** *126*, 11889-11899.
52. Lu, T., Multiwfn Manual, version 3.7(dev), Section 4.8.5, available at http://sobereva.com/multiwfn.

53. Zhang, R.; Adsetts, J. R.; Nie, Y.; Sun, X.; Ding, Z., Electrochemiluminescence of nitrogen- and sulfur-doped graphene quantum dots. *Carbon* **2018,** *129*, 45-53.
54. Hesari, M.; Swanick, K. N.; Lu, J.-S.; Whyte, R.; Wang, S.; Ding, Z., Highly Efficient Dual-Color Electrochemiluminescence from BODIPY-Capped PbS Nanocrystals. *J. Am. Chem. Soc.* **2015,** *137*, 11266-11269.
55. Sivula, K., Mott–Schottky Analysis of Photoelectrodes: Sanity Checks Are Needed. *ACS Energy Lett.* **2021,** *6*, 2549-2551.
56. Peng, G.; Albero, J.; Garcia, H.; Shalom, M., A Water-Splitting Carbon Nitride Photoelectrochemical Cell with Efficient Charge Separation and Remarkably Low Onset Potential. *Angew. Chem. Int. Ed.* **2018,** *57*, 15807-15811.
57. Frisch, M. J.; Trucks, G. W.; Schlegel, H. B.; Scuseria, G. E.; Robb, M. A.; Cheeseman, J. R.; Scalmani, G.; Barone, V.; Petersson, G. A.; Nakatsuji, H.; Li, X.; Caricato, M.; Marenich, A. V.; Bloino, J.; Janesko, B. G.; Gomperts, R.; Mennucci, B.; Hratchian, H. P.; Ortiz, J. V.; Izmaylov, A. F.; Sonnenberg, J. L.; Williams; Ding, F.; Lipparini, F.; Egidi, F.; Goings, J.; Peng, B.; Petrone, A.; Henderson, T.; Ranasinghe, D.; Zakrzewski, V. G.; Gao, J.; Rega, N.; Zheng, G.; Liang, W.; Hada, M.; Ehara, M.; Toyota, K.; Fukuda, R.; Hasegawa, J.; Ishida, M.; Nakajima, T.; Honda, Y.; Kitao, O.; Nakai, H.; Vreven, T.; Throssell, K.; Montgomery Jr., J. A.; Peralta, J. E.; Ogliaro, F.; Bearpark, M. J.; Heyd, J. J.; Brothers, E. N.; Kudin, K. N.; Staroverov, V. N.; Keith, T. A.; Kobayashi, R.; Normand, J.; Raghavachari, K.; Rendell, A. P.; Burant, J. C.; Iyengar, S. S.; Tomasi, J.; Cossi, M.; Millam, J. M.; Klene, M.; Adamo, C.; Cammi, R.; Ochterski, J. W.; Martin, R. L.; Morokuma, K.; Farkas, O.; Foresman, J. B.; Fox, D. J. *Gaussian 16 Rev. C.01*, Wallingford, CT, 2016.
58. Lu, T.; Chen, F., Multiwfn: A multifunctional wavefunction analyzer. *J. Comput. Chem.* **2012,** *33*, 580-592.